Microstructural evolution of layered K-doped $RuCl_3$ during annealing traced by thermogravimetric analysis and 3D electron diffraction

Vinokurova, E.; Knorr, M.; Efimova, A.; Ovchinnikov, A.; Schmidt, P.; Büchner, B.; Isaeva, A.; Roslova, M.

DOI
10.1002/zaac.202300141

Publication date
2023

Document Version
Final published version

Published in
Zeitschrift fur Anorganische und Allgemeine Chemie

Journal of Inorganic and General Chemistry
ZAAC
Zeitschrift für anorganische und allgemeine Chemie
www.zaac.wiley-vch.de
RESEARCH ARTICLE
Check for updates
DOI: 10.1002/zaac.202300141

Special Collection

Microstructural evolution of layered K-doped $RuCl_3$ during annealing traced by thermogravimetric analysis and 3D electron diffraction

Ekaterina Vinokurova,[a, c] Monika Knorr,[b] Anastasia Efimova,[b] Alexander Ovchinnikov,[c] Peer Schmidt,[b] Bernd Büchner,[a] Anna Isaeva,[a, d] and Maria Roslova*[a]

Dedicated to Professor Michael Ruck on the Occasion of His 60th Birthday

Nanoscale phase separation was induced in the K-doped $RuCl_3$ van der Waals material by annealing, and studied with the goal to find a natural design strategy for the formation of two-dimensional architectures as an alternative to the costly and time-consuming experimental artificial growth methods. Phase conversion was traced by means of thermogravimetric analysis combined with mass spectrometry. The local crystal structure of co-existing $K_3Ru_2Cl_9$ domains with the sizes of about 100 nm was solved by 3D electron diffraction.

Introduction

In recent years, there has been a great effort to create artificial heterostructures and nanoarchitectures using vertically stacked two-dimensional (2D) van der Waals (vdW) layered materials.[1–3] Similar to those in bulk materials, defects or a lattice mismatch in 2D heterostructures can induce strains that distort the shape of individual layers or induce twists between the layers. However, the impact of defects is exacerbated with reduced dimensionality which may result in unique architectures, such as e.g. supertwisted spirals of layered materials,[4,5] nanoscrolls, nanotubes and many others.[6]

Fabrication of heterostructures has relied mostly on artificial growth methods, such as mechanical exfoliation and re-assembly, or chemical vapor deposition (CVD). Especially for the CVD method, all synthesis parameters have to be extremely precise since the desired architectures are often thermodynamically unfavorable.[7] However, during annealing, many solids naturally undergo formation of morphologic microstructures or a phase separation, when, below a certain critical temperature, the components separate into distinct homogeneous regions with different physical and chemical properties. These precipitates may already have a complex spatial organization, e.g. 3D nanoscale strips in the alkali-doped iron selenides[8,9] or arrays of nanocrystals coherently embedded into a semiconductor matrix.[10] Moreover, creating boundaries between chemically distinct but structurally related phases may remarkably affect physical properties. For example, increased dislocation densities and decreasing grain size in thermoelectric materials may lead to reduced lattice thermal conductivity.[11,12] In semiconductors, such as GaAs, GaN, ZnTe, or elemental semiconductors, e.g., Ge doped with transition metal ions (Cr, Mn, or Fe), the formation of self-assembled quantum dots or nano-islands with the composition differing from that of the matrix is strictly correlated with the presence of high-T_C ferromagnetism, and has been extensively studied for potential applications in low-current semiconductor lasers, solar cells, single-photon emitters and detectors, quantum processors, and memories.[13] Spinodal decomposition is proposed for stabilizing self-assembled interfaces between topological insulators by combining layers of iso-structural $TlBiX_2$ (X = S, Se, Te) materials. The tuning may induce phenomena such as topological interface states, non-trivial spin texture, and Rashba-like states.[14] The broad variety of domains forming at micro- or nanoscale during the chemical decomposition poses significant challenges to elucidating their crystal structure, which is essential to understand their chemical and physical behavior. Conventional in-house structure characterization techniques, such as X-ray diffraction, often prove impractical in addressing this issue. To overcome these

[a] E. Vinokurova, Prof. Dr. B. Büchner, Prof. Dr. A. Isaeva, Dr. M. Roslova
Leibniz Institute for Solid State and Materials Research Dresden
Helmholtzstraße 20, 01069 Dresden, Germany
E-mail: m.roslova@ifw-dresden.de
[b] M. Knorr, Dr. A. Efimova, Prof. Dr. P. Schmidt
Brandenburgische Technische Universität Cottbus-Senftenberg
Universitätsplatz 1, 01968 Senftenberg, Germany
[c] E. Vinokurova, Dr. A. Ovchinnikov
Technische Universität Dresden
Haeckelstraße 3, 01062 Dresden, Germany
[d] Prof. Dr. A. Isaeva
University of Amsterdam
Science Park 904, 1098 XH Amsterdam, The Netherlands

Supporting information for this article is available on the WWW under https://doi.org/10.1002/zaac.202300141

This article is part of a Special Collection dedicated to Professor Michael Ruck on the occasion of his 60th birthday. Please see our homepage for more articles in the collection.

challenges and achieve structural elucidation at the nanoscale, we have employed three-dimensional electron diffraction (3D ED). This advanced method has gained recognition for its ability to determine the crystal structure of individual micro- and nanosized crystals.

This study contributes to the understanding of the boundary structures arising in K-doped $RuCl_3$ through a decomposition process. The system's choice was motivated by an existing scope of studies showing that electrochemical intercalation of potassium into the $RuCl_3$ van der Waals material is very feasible and yields environmentally stable products. It has been tackled in the literature since the 1980's. Previous investigations focused largely on the reaction mechanisms, pH- and temperature dependencies, and the optical, optoelectronic, and transport properties of the intercalation products, e.g. $K_xRu_2Cl_6$ ($1 < x < 2$) and to a significantly lesser extent on its crystallographic peculiarities.[15–19] Whereas our structural studies of the $K_xRu_2Cl_6$ intercalates and, in particular, of KRu_2Cl_6 are described elsewhere,[20,21] this work examines the thermal decomposition of the K-intercalated $RuCl_3$ and compares it to the parent α-$RuCl_3$ compound. We find that decomposition of the intercalate markedly differs from that of α-$RuCl_3$, and notably, is accompanied by a nanoscale phase separation. Further, we focus on the detailed characterization of a new decomposition product by employing 3D ED, and a combination of the powder X-ray diffraction (pXRD), the thermogravimetric analysis combined with the mass spectrometry (TGA-MS), and the high resolution transmission electron microscopy (HRTEM). We unveil the crystal structure of a distinct $K_3Ru_2Cl_9$ domain arising from the decomposition process. The accurate structure elucidation helps to attain a more profound knowledge of the decomposition process in general.

Results and Discussion

After a rapid, high-temperature annealing of K-doped $RuCl_3$ following the procedure described in the Experimental Section, we analyzed the sample by scanning electron microscopy (SEM) combined with energy dispersive X-ray analysis (EDX). SEM images of the annealed and non-annealed samples are shown in Figure 1.

The average quantitative composition of the samples before and after the annealing was determined by EDX. Annealing under vacuum leads to a drop of oxygen content in the specimen from approx. 16(5) at% to approx. 6(1) at%, but it also affects the K:Ru:Cl ratio in the sample, which changes from 0.77(8):1:3.03(10) to 0.55(3):1:2.45(7). In order to get further insight into it, we went for local analysis by TEM and 3D ED, described below in the manuscript.

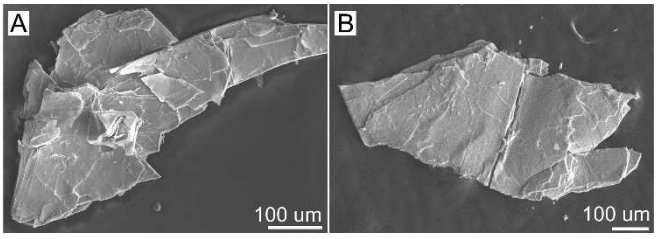

Figure 1. a) A typical SEM image of the K-doped $RuCl_3$ before thermal treatment; b) An SEM image of the specimen annealed under vacuum.

A transmission electron microscopy (TEM) investigation reveals an inherent nanoscale phase separation in the annealed K-doped $RuCl_3$, visible at high resolution in the form of small, nanometer-sized plates in the annealed sample, not present in the non-annealed one. Thus, phase separation was induced in the K-doped $RuCl_3$ by annealing. To collect the structural information from these small domains, we have implemented 3D ED following the cRED protocol,[22] which allows structure reconstruction from a sequence of electron diffraction patterns recorded at different specimen tilt angles. TEM parallel beam nanoprobe mode was used to minimize the data collection region. Figure 2 shows a typical HRTEM image of the co-existing areas and their characteristic fast Fourier transform images (FFT). Region B is more extended, and its FFT pattern shows a distorted hexagonal array. In contrast, Region A is a relatively small domain embedded in the matrix of Region B, and its FFT pattern exhibits several rows of spots.

Small round particles seen on the surface are mainly Ru nanoparticles, as evidenced by EDX, whereas plate-like particles represent an unknown crystalline contamination.

We found out that the characteristic fast Fourier transform image from Region B is consistent with an ED of {001} crystal planes in the crystal structure of the rhombohedral $K_xRu_2Cl_6$ intercalate, in line with our pXRD results (see below).

Next, we analyzed the reconstructed 3D reciprocal space from Region A, demonstrating rows of reflections with a *d*-spacing of 1.7 nm in FFT. This *d*-spacing is present neither in $K_xRu_2Cl_6$ nor in the parent α-$RuCl_3$. The domain of the unknown phase is oriented relatively close to a zone-axis and thanks to it is clearly visible among the surrounding matrix of $K_xRu_2Cl_6$ due to a HRTEM diffraction contrast. A slightly larger domain of the same phase with sizes of about 50×70 nm seen in the direct space image in Figure 3 was used further for the 3D ED data collection.

Although the dataset was noisy, a hexagonal unit cell with lattice parameters $a = 6.717(3)$ Å, $c = 17.096(2)$ Å, $V = 668.0(2)$ Å^3 was found by the RED$_p$ cell finding algorithm from the 3D ED experiment. The only condition $l = 2n$ was found in the 00*l* reflection row, suggesting possible space groups: $P6_3mc$, $P\bar{6}2c$ and $P6_3/mmc$. Similar cell parameters are commonly adopted by halides crystallizing in a derivative of the hexagonal perovskite (ABX_3) structure, with *B* cations occupying only two-thirds of the octahedral site (i.e., $A_2B_2X_9$), such as for example $Cs_3B_2Cl_9$ (B = Mo, Fe, Cr).[23,24] An isostructural $Cs_3Ru_2Cl_9$ compound was described by Darriet.[25] Early mentions of $K_3Ru_2Cl_9$ as a precursor for synthesizing diruthenium complexes[26–28] did not include any crystallographic characterization. In the PhD thesis of S. Hartwig (Universität Bayreuth), the $K_3Ru_2Cl_9$ phase was isolated as bulk and its cell parameters were estimated from pXRD, but no crystal structure model was provided.[29] Our

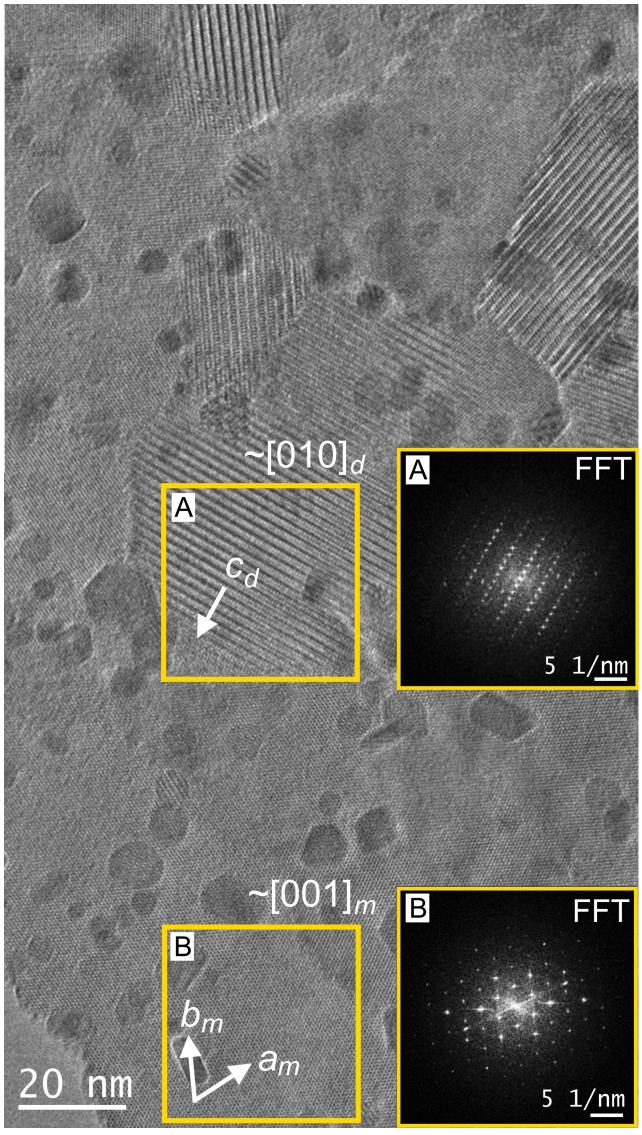

Figure 2. A typical HRTEM image of the annealed K-doped $RuCl_3$ specimen showing co-existing crystalline domains. Matrix domain (*m*) is imaged along the [001] direction, domains of $K_3Ru_2Cl_9$ (*d*) – close to the [010] direction in the $K_3Ru_2Cl_9$ crystal structure.

ab-initio structure solution from the 3D ED data confirmed that $K_3Ru_2Cl_9$ is isostructural to $Cs_3Ru_2Cl_9$ (sp. gr. $P6_3/mmc$). Out of 2294 reflections collected, 217 were unique, $R_{int}=0.289$. The resolution cutoff of 0.79 Å was chosen based on Ref. [30] ($CC_{1/2}$ = 98.4 and 88% in the resolution shells 0.83 and 0.79 Å, correspondingly), and the resulting total data completeness was 66.1% and $I/\sigma=4.73$. The refinement based on 217 reflections and 19 parameters converged to $R=0.179$ and $R_w=0.454$. Details of the refinement are given in Table 1. CCDC 2274900 contains the crystallographic data for the solved $K_3Ru_2Cl_9$ structure. Due to a strong peak overlapping (see Figure 6) and small size of the domains, this phase cannot be reliably identified from pXRD, however, it can be discovered by 3D ED.

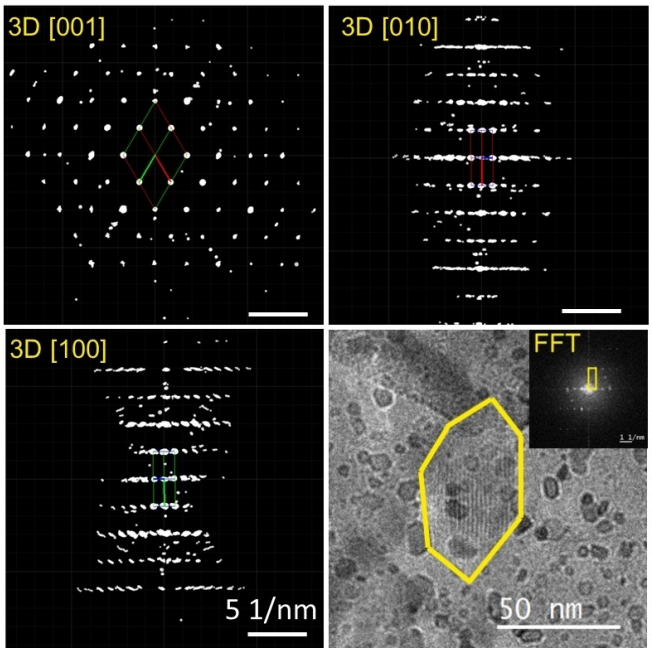

Figure 3. 3D ED dataset taken from a single domain of the annealed specimen revealing a hexagonal unit cell with $a=6.717(3)$ Å, $c=17.096(2)$ Å. The scalebar 5 nm^{-1} is the same for all ED images.

Table 1. Crystal data and structure refinement for $K_3Ru_2Cl_9$.

Empirical formula	$K_3Ru_2Cl_9$
Formula weight	638.51
Temperature/K	293(2)
Crystal system	hexagonal
Space group	$P6_3/mmc$
a/Å	6.717(3)
c/Å	17.096(2)
Volume/Å^3	668.0(2)
Z	2
ϱ_{calc}/g cm^{-3}	3.171
Crystal size	50×70 nm
Radiation	electrons with $\lambda=0.0197$ Å
2Θ range for data collection/°	0.194 to 1.432
Reflections collected	2294
Independent reflections	217 [$R_{int}=0.289$, $R_{sigma}=0.160$]
Data/restraints/parameters	217/0/19
Goodness-of-fit on F^2	1.606
Final *R* indexes [$I\geq 2\sigma(I)$]	$R_1=0.179$, $wR_2=0.454$
Final *R* indexes [all data]	$R_1=0.208$, $wR_2=0.467$
Largest diff. peak/hole/e Å^{-3}	1.67/−2.37

The structure is characterized by isolated dimeric $[Ru_2Cl_9]^{3-}$ units, Figure 4A. In contrast to $K_xRu_2Cl_6$ or α-$RuCl_3$, which host layers of edge-sharing $[RuCl_6]$ octahedra with the central Ru^{3+} ions forming a honeycomb lattice, the structure of $[Ru_2Cl_9]^{3-}$ units is not 2D anymore, and results from the sharing of a trigonal face between two $[RuCl_6]$ octahedra. The Ru atoms are located close to the centers of their respective coordination octahedra, with the shortest Ru–Ru distance of 2.59(3) Å

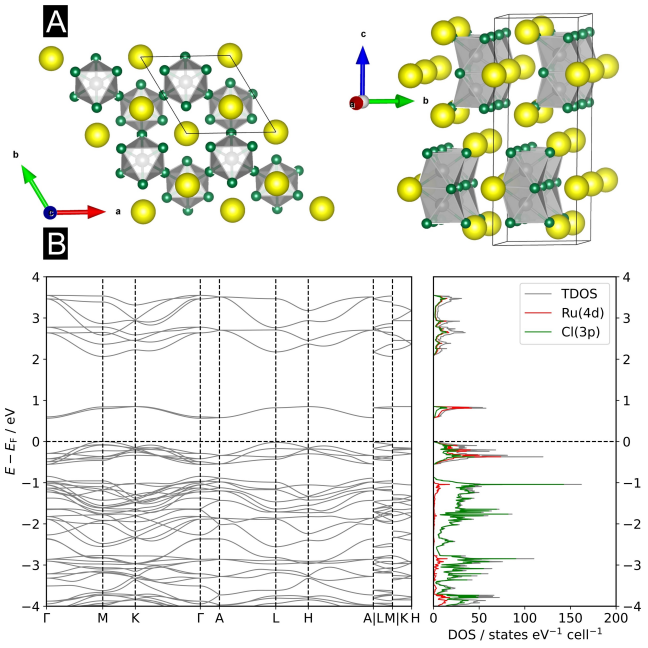

Figure 4. (A) Crystal structure of $K_3Ru_2Cl_9$. K, Ru and Cl atoms are shown in yellow, grey and green, respectively. (B) Electronic band structure (left) and density of states (DOS, right) for $K_3Ru_2Cl_9$. Selected projected contributions to the DOS are indicated.

between the atoms in the adjacent octahedra. The Ru–Cl bond lengths are in the range of 2.25–2.29 Å.

To gain insight into the electronic properties of $K_3Ru_2Cl_9$, which was present in our samples only as nanoscale domains, we carried out first-principle calculations using the experimentally determined crystal structure. Due to the $4d^5$ electronic state of Ru^{3+} in $K_3Ru_2Cl_9$, a magnetic ground state can be anticipated. Therefore, we started our calculations by considering a ferromagnetic structure. However, the local magnetic moments on the Ru atoms converged to less than 10^{-5} μ_B, suggesting the absence of localized magnetism. A calculation for an antiferromagnetic arrangement also converged to negligible magnetic moments on the Ru sites, thus confirming a non-magnetic ground state. This result aligns with the experimental observations on the related compound, $Cs_3Ru_2Cl_9$, which only showed a weak paramagnetic response.[25]

The lack of localized magnetism is related to the formation of a Ru–Ru bond in the $[Ru_2Cl_9]^{3-}$ dimers, resulting in a singlet ground state. The observed weak paramagnetism at finite temperatures is ascribed to the population of the excited triplet state. The band structure and electronic density of states for $K_3Ru_2Cl_9$ are shown in Figure 4B. The ground state is hallmarked by an indirect bandgap of about 0.56 eV. Due to the ionic nature of the K–Cl interaction and the accompanying electron transfer from the K atoms, the contribution of the K valence states around and below the Fermi level (E_F) is small. The DOS region below the E_F mainly comprises the hybridized Ru(4d) and Cl(3p) states. The localized bands right above the Fermi level consist predominantly of the unoccupied Ru(4d) e_g states.

Following the inherent phase separation and identification of nanometer-sized platelets with the composition $K_3Ru_2Cl_9$ in the TEM after rapid annealing, an investigation was carried out to determine whether the formation of this phase also occurs in the course of the thermal decomposition of $K_xRu_2Cl_6$.

At first, a $K_xRu_2Cl_6$ sample obtained by electrochemical intercalation was measured by pXRD (Figure 6). The most prominent reflections for the non-annealed sample can be indexed in a rhombohedral cell with the lattice parameters $a \approx 3.46(2)$ Å, $c \approx 24.96(2)$ Å. This structure adopting the space group *R*3*m* is the subject of our other work that deals with the structural aspects of the non-annealed $K_xRu_2Cl_6$ intercalates ($1 < x < 2$).[20,21] The structure preserves the BiI_3-type layers of edge-sharing $[RuCl_6]$ octahedra with the central Ru^{3+} ions forming a honeycomb lattice and additionally hosts a varying amount of K atoms in the interlayer space. Despite the increased ionic interaction between the layers via K cations, the $K_xRu_2Cl_6$ structure is a subject to multiple stacking faults due to the sliding of the layers with respect to each other. It is worth noting that for the sample before the TG, the first pXRD peak splits into two, with the *d* values of ~8.32 Å and ~8.21 Å, indicating an intrinsic inhomogeneous potassium distribution in the sample.

The thermal behavior of the $K_xRu_2Cl_6$ ($x = 1$–2) samples with variable potassium doping was investigated by thermogravimetric analysis coupled with mass spectrometry (TGA-MS) to get further information about the gaseous decomposition products formed.

As references, $RuCl_3$ and KCl were also analyzed by TGA under the same conditions. The obtained TG curves and their first derivatives (DTG) are shown in Figure 5A. The measurement was stopped at certain temperatures to identify the steps that occur during the heating from room temperature to 1100 °C (Figure 5B). An optical examination and identification of the crystalline phases by powder diffraction (pXRD) of the crucible residue (see Figure 5B), were performed. Diffractograms and the assignment of the crystalline phases can be taken from Figure 6.

The thermal decomposition of $K_xRu_2Cl_6$ ($x = 1$–2) runs in six defined steps. The first step starts at $\vartheta_{onset,DTG} = 473$ °C ($\vartheta_{peak,DTG} = 545$ °C) and ends with a mass loss of 17.05 % at 568 °C. Up to 473 °C, no gaseous species could be detected by MS (Figure 5B). It can therefore be assumed that the $K_xRu_2Cl_6$ ($x = 1$–2) under investigation is completely anhydrous ($m/z = 17$, 18). Atomic chlorine species of both isotopes, ^{35}Cl and ^{37}Cl, were detected in the ratio 1 to 3 at the beginning of the decomposition of $K_xRu_2Cl_6$, while the molecular chlorine species did not occur. The observed mass traces of ^{36}HCl and ^{38}HCl in the ratio of 1 to 3 can be explained by the reaction of formed gaseous $^{35}Cl/^{37}Cl$ with the small traces of water (< 0.02 ppm) from the purge gas.

According to the evaporation behavior of pure α-$RuCl_3$, simulated by detailed Calphad-modelling,[31] it can be assumed, that the first TG step, starting from 473 °C, leads to partial decomposition of $K_xRu_2Cl_6$ under slight loss of chlorine and small amounts of $RuCl_3$, thus leading to an enrichment of potassium. The early start of decomposition, compared to the

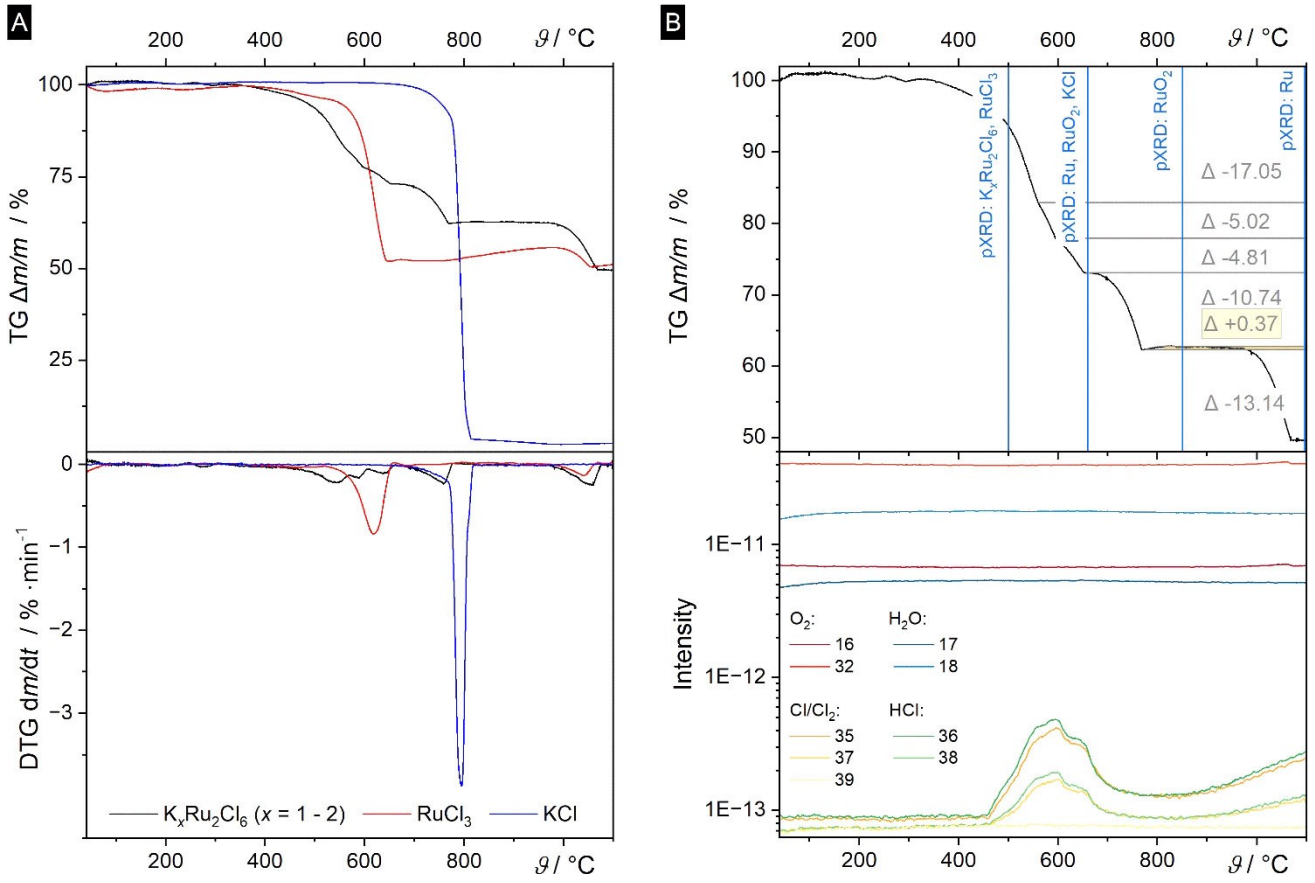

Figure 5. Analysis of the thermal decomposition of $K_xRu_2Cl_6$ by TGA-MS under helium atmosphere at a heating rate of 1 K·min^{-1} (A): TG-, DTG-curves of $K_xRu_2Cl_6$ (black), $RuCl_3$ (red) and KCl (blue), and (B): TG-curve of $K_xRu_2Cl_6$ with the identified mass changes (grey), phase compositions from pXRD (blue) of the crucible residue at 500 °C, 660 °C, 850 °C and 1100 °C and the corresponding MS-spectrum of formed gaseous species over the whole temperature range.

pure $RuCl_3$ phase (see Figure 5A), hints to a metastable state of $K_xRu_2Cl_6$.

Powder XRD of the residue after stopping the TG measurement at 500 °C showed a presence of α-$RuCl_3$ and presumably a potassium-rich $K_xRu_2Cl_6$ phase. Figure 6 shows that the most prominent reflections in the diffractogram at 500 °C fit well to their (00*l*) series. Both α-$RuCl_3$ and intercalated $K_xRu_2Cl_6$ exhibit high texture effects due to their layered morphology. Compared with the non-annealed sample, the *d*-spacing for the first pXRD peak increases to ~8.52 Å. It presumably corresponds to the $K_xRu_2Cl_6$ intercalated phase with an increased *c*-axis parameter and higher K-content. Interestingly, the appearance of α-$RuCl_3$ phase at 500 °C might result either from non-uniform intercalation or might indicate redistribution of K in the sample, e.g. formation of regions rich in the K-content, and deintercalated regions.

The first decomposition step is immediately followed by the second and third decomposition steps, thus forming an actually long drawn, but segmented decomposition profile. The second decomposition step of $K_xRu_2Cl_6$ ($x = 1$–2) could be determined at $\vartheta_{onset,DTG} = 497$ °C ($\vartheta_{peak,DTG} = 589$ °C) with the mass loss of 5.02 % and the end temperature at 607 °C. The third mass stage starts at $\vartheta_{onset,DTG} = 575$ °C ($\vartheta_{peak,DTG} = 637$ °C) with a mass loss of 4.81 % and ends at 661 °C. Here, the intercalated phase completely decomposes, forming KCl and Ru components resulting from the incongruent decomposition under release of chlorine.

This behavior completely agrees with the one of pure $RuCl_3$, which decomposes starting from $\vartheta_{onset,DTG} = 565$ °C ($\vartheta_{peak,DTG} = 619$ °C).

According to the calculated gas phase composition,[31] mainly Cl (from Cl_2) as gaseous species could be identified with the MS of $RuCl_3$, and finally, for the investigated samples $K_xRu_2Cl_6$ ($x = 1$–2) as well. $RuCl_3$ could not be identified in the MS, as small amounts of the gas species already condense in the transfer line. The pXRD analysis of the crucible residue of $K_xRu_2Cl_6$ ($x = 1$–2) decomposed up to 660 °C indicates the formation of the following phases: KCl, Ru, and RuO_2 (Figure 6). Examination of the crucible residue of $RuCl_3$ after the first mass step (700 °C) resulted in the identification of Ru and RuO_2 (Figure 6). Thus, within the second and third mass stages further decomposition of the potassium-rich $K_xRu_2Cl_6$ phase to KCl(s) and decomposition of $RuCl_3$(s) to Ru(s) and Cl_2(g) occurs. The detection of RuO_2(s) in the pXRD (Figure 6) can be explained by

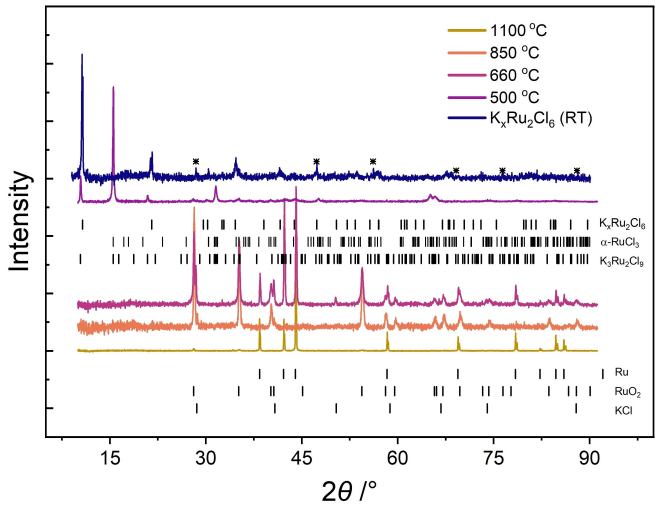

Figure 6. Experimental powder X-ray diffraction patterns (CuK_α) of $K_xRu_2Cl_6$ before TG and residuals after TG experiments stopped at 500, 660, 850 and 1100 °C. The peak positions of Ru, RuO_2, KCl and $RuCl_3$ are taken from PDF 00-006-0663, PDF 01-070-2662, PDF 00-001-0790, and ICSD 258397 (Ref. [32]), correspondingly, and are indicated by black ticks. The theoretical peak positions of the $K_3Ru_2Cl_9$ phase are given for comparison, calculated according to Ref. [29] Asterisks show the peak positions of the Si standard, mixed with the $K_xRu_2Cl_6$ sample before TG.

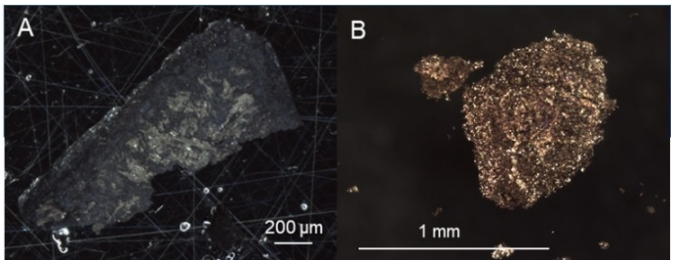

Figure 7. Optical investigation of the residues after TG-measurement (A) metallic, grey crucible residue after TGA measurement of $K_xRu_2Cl_6$ ($x = 1–2$) after 850 °C, (B) gold-colored porous residue of $K_xRu_2Cl_6$ ($x = 1–2$) after heat treatment up to 1100 °C.

the reaction of Ru with the small traces of oxygen (< 0.01 ppm) in the He purge gas stream.

The fourth decomposition step with a mass loss of 10.74% is observed in the temperature range from 662 °C to 773 °C ($\vartheta_{onset,DTG} = 693$ °C, $\vartheta_{peak,DTG} = 759$ °C). No signals from ^{35}Cl and ^{37}Cl could be detected in this temperature interval by MS. The pXRD of the sample decomposed up to 850 °C showed the crystalline phases of Ru and RuO_2. The reference measurement of the pure KCl shows an initial shoulder at $\vartheta_{onset,DTG} = 701$ °C, with a subsequent sharp loss of mass at $\vartheta_{onset,DTG} = 775$ °C ($\vartheta_{peak,DTG} = 795$ °C). This behavior corresponds to the initial melt of the KCl, with the following immediate sublimation to KCl(g). Here again, the released $KCl_{(g)}$ mainly condenses in the transfer line to the MS. Nevertheless, in agreement with the onset temperatures of the melt and subsequent vaporization of KCl as well as the results of pXRD, the fourth mass stage of thermal decomposition of $K_xRu_2Cl_6$ ($x = 1–2$) can be attributed to the sublimation of KCl.

The fifth mass step of $K_xRu_2Cl_6$ ($x = 1–2$) reveals a slight mass increase of +0.37% in a temperature range from 773 °C to 883 °C, which is also indicated in the reference measurement of pure $RuCl_3$. Analysis of the solid residue of the sample of $K_xRu_2Cl_6$ ($x = 1–2$) in the crucible after 850 °C by pXRD shows the formation of RuO_2 (Figure 6). An optical examination of the solid (Figure 7A) confirms formation of grey RuO_2 layer. Thus, it is probable that the formed Ru was oxidized by the small traces of oxygen in the He purge gas flow.

The sixth and last mass step shows a mass loss of 13.14%. The decomposition step proceeds in the temperature range from 883 °C to 1100 °C with $\vartheta_{onset,DTG} = 989$ °C and $\vartheta_{peak,DTG} =$ 1060 °C. This decomposition step corresponds to the third effect of the pure $RuCl_3$ ($\vartheta_{onset,DTG} = 987$ °C, $\vartheta_{peak,DTG} = 1039$ °C). The pXRD of the crucible residue of $K_xRu_2Cl_6$ and $RuCl_3$ obtained at temperature up to 1100 °C reveals only reflections of Ru (Figure 6). It is additionally proven by the formation of gold-colored porous solid after heating of $K_xRu_2Cl_6$ up to 1100 °C (Figure 7B). Concluding, the last step can be assigned for both $K_xRu_2Cl_6$ and $RuCl_3$ to the reduction of the previously formed RuO_2 with the formation of Ru. Similar behavior of mass increase by oxidation with the oxygen from the purge gas and subsequent reduction has already been described for rhodium.[33]

Albeit exact quantification of the observed decomposition path was hindered due to the uncertainty of the initial solid and the complex composition of the gas phase during the thermal treatment, observations indicate occurrence of mainly Cl_2(g) and KCl(g), but simultaneously release of $RuCl_3$(g) and O_2(g), too. This study concludes that $K_3Ru_2Cl_9$ does not form, at least not as a bulk phase with visible contributions to pXRD and TGA, upon thermal decomposition of K-doped $RuCl_3$ at the heating rate of 1 K·min^{-1}. Nanoscale phase separation we report here is thus, presumably, the result of a non-equilibrium process facilitated by rapid, high-temperature heating.

Conclusions

In this paper we study the processes of thermal decomposition of K-doped $RuCl_3$ by combining the pXRD, TGA-MS, HRTEM and electron diffraction findings. It was shown that the decomposition of K-doped $RuCl_3$ to Ru and KCl(g) occurs in a multi-step fashion in the temperature range 400–1100 °C and is accompanied by elimination of Cl_2. In the temperature range approx. 500–600 °C, a nanoscale phase separation can be naturally induced by rapid, out-of-equilibrium heating, revealing itself in HRTEM as structurally different plate-like domains embedded into the $K_xRu_2Cl_6$ matrix. The crystal structure of the domains was solved and refined against 3D ED data. The structure was found to adopt the sp.gr. $P6_3/mmc$ with the unit-cell parameters $a = 6.717(3)$ Å, $c = 17.096(2)$ Å, $V = 668.0(2)$ Å^3 and has a general formula $K_3Ru_2Cl_9$. The comprehensive nano-characterization has enabled us to put on a firmer basis the

origin of crystallographic and chemical phase separation observed during annealing of the K-doped $RuCl_3$ intercalate. Our study demonstrates the power of 3D ED in tackling the challenges of structural elucidation in systems undergoing nanoscale phase separation, contributing to the advancement of scientific knowledge and potential practical applications in the field of materials research.

Experimental Section

Large crystals of $RuCl_3$ for intercalation were grown by the chemical vapor transport technique as described elsewhere.[34,35] The mechanism of CVT for α-$RuCl_3$ is described in details in Ref. [31] α-$RuCl_3$ used for thermogravimetric analysis was purchased from Aldrich Chemistry (45–55 % Ru content), and purified according to Froeschke et al.[36] Intercalation was performed at room temperature in a three-electrode electrochemical cell filled with 0.5 M KCl (99 %, Sigma-Aldrich) aqueous solution. A rectangular piece of α-$RuCl_3$ with the sizes of about 2×3 mm was placed onto the Pt mesh (99.9 %, Goodfellow GmbH) that was then folded around the crystal and clamped. A Pt plate (99.99 %, Goodfellow GmbH) was used as the counter (CE) electrode and an Ag/AgCl wire as a pseudo-reference electrode. Metrohm Autolab PGSTAT204 potentiostat with the Nova 2.1.5 software was used for the control of the measurements and for the acquisition of the data. Intercalation was performed in a chronoamperometric regime by applying a constant potential of −0.6 V vs Ag/AgCl pseudo-reference electrode for 5 minutes. After the electrochemical treatment was accomplished, the K-doped $RuCl_3$ crystal was washed with distilled water and dried in air for a few days. Annealing of the K-doped $RuCl_3$ crystal was conducted in a quartz tube heated by a conventional hydrogen burner under dynamic vacuum (10^{-3} mbar) for several seconds.

The thermal decomposition of synthesized $K_xRu_2Cl_6$, KCl (99,5 %, Carl Roth GmbH + Co. KG), and $RuCl_3$ (45–55 % Ru content, Aldrich Chemistry, purified according to Froeschke et al.[36]) was investigated with a simultaneous thermal analyzer STA 449 F3 Jupiter combined with a mass spectrometer QMS 403 D Aëolos (TGA/DTA-MS) manufactured by NETZSCH. The measurements were carried out in the temperature range from 40 °C to 1100 °C at a heating rate of 1 $K \cdot min^{-1}$ under the helium flow with a rate of 50 $cm^3 \cdot min^{-1}$ and 20 $cm^3 \cdot min^{-1}$ inert gas flow for the balance. Alumina crucibles without cover were used. The adapter head of the STA was heated to 300 °C as well as the transfer line between STA and QMS and the inlet of QMS. Initially, the bargraph and after MID measuring mode by QMS experiments were fulfilled. The residues obtained from TGA at different temperatures were examined microscopically in more detail using Stemi 2000-C from Zeiss. The images were taken with the Motic Moticam 5 digital camera from the manufacturer's CMOS sensor. For residues with depth, multiple photos were taken at different focus distances to maintain the depth of field and merged into one image using Helicon-Focus software.

Scanning electron microscopy (SEM) images were taken on a Hitachi SU8020 microscope equipped with a triple detector system. Energy-dispersive X-ray spectroscopy (EDX) measurements were conducted on the Hitachi's microscope using an X–Max^N Silicon Drift Detector (SDD) (Oxford Instruments) with $U_e = 20$ kV.

The pXRD pattern of $K_xRu_2Cl_6$ before the thermogravimetric analysis was taken on Malvern PANalytical Empyrean diffractometer with a curved Ge(111)-monochromator, whereas other diffractograms were recorded using a BRUKER D2 instrument with an accelerating voltage of 30 kV and filament current of 10 mA, equipped by a nickel filter and a built-in detector (LynxEye, semiconductor strip detector system (192 strips = 3°(2θ)). The measurements were performed with Cu-K_α radiation ($\lambda = 1.54056$ Å) in the reflection mode in the ranges $5° \leqslant 2\theta \leqslant 90°$ (Empyrean) and $10° \leqslant 2\theta \leqslant 90°$ (BRUKER D2). A sample holder with silicon single crystal was used for the measurement. All measurements were done at room temperature under an air atmosphere. After the acquisition, the obtained diffractograms were analyzed for the contained phases using EVA software. Reference samples from the ICDD database were used for phase identification.

The specimen for 3D ED and HRTEM experiments was prepared by crushing a crystal of the annealed K-doped $RuCl_3$ in a mortar, followed by suspending it in ethanol. Drops of the suspension were then dried on carbon-film copper grids (Cu150P Okenshoji Co., Ltd) at room temperature. 3D ED patterns and HRTEM images were collected on a probe and image C_S – corrected Themis Z microscope operating at 300 kV and equipped with a Gatan OneView camera. *In-situ* data capture mode with 1024×1024 pixels resolution (binning ×4) was employed. Data acquisition was performed using a single-tilt tomography holder, following the cRED protocol,[22] and was controlled by InsteaDMatic script.[37] ED frames were collected over a tilt range of ±40° with a rotation speed ~0.43°/s, the exposure time was 0.3 s. Diffraction frames were processed with the XDS.[38] The structure was solved by dual-space phasing in SHELXT[39] and refined by full-matrix least-squares method on F^2 with SHELXL[40] using Olex2 software.[41]

Electronic structure calculations on the density functional theory level (DFT) were performed with the FPLO21.00 code.[42] The Perdew-Wang (PW92) flavor of the local density approximation (LDA) functional was used.[43] To account for the electronic correlations, the LDA + U scheme was applied, with the on-site Coulomb repulsion $U = 1.5$ eV and Hund's exchange $J = 0.3$ eV, as has been used for α-$RuCl_3$ in previous publications.[44,45] The Brillouin zone was sampled by a 8×8×3 k-point grid after checking for convergence.

Acknowledgements

We cordially thank Almut Pöhl (IFW Dresden) for the help with TEM sample preparation. The Electron Microscopy Centre (EMC) at the department of Materials and Environmental Chemistry, Stockholm University is acknowledged for providing time for 3D ED data collection. Financial support from DFG is acknowledged through DFG CRC 1143 (Project 247310070) and DFG Project 419941440. A.E. and M.K. acknowledge the support by the European Regional Development Fund (ERDF-Brandenburg, Project 85006795 and Project 80155970, see: www.efre.brandenburg.de). Open Access funding enabled and organized by Projekt DEAL.

Conflict of Interest

The authors declare no conflict of interest.

Data Availability Statement

The data that support the findings of this study are available from the corresponding author upon reasonable request.

Keywords: electrochemical intercalation · K-doped $RuCl_3$ · annealing · nanoscale phase separation · thermogravimetric analysis · 3D ED

[1] A. Castellanos-Gomez, X. Duan, Z. Fei, H. R. Gutierrez, Y. Huang, X. Huang, J. Quereda, Q. Qian, E. Sutter, P. Sutter, *Nat. Rev. Methods Primers* **2022**, *2*, 1–19.
[2] K. S. Novoselov, A. Mishchenko, A. Carvalho, A. H. C. Neto, *Science* **2016**, *353*, aac9439.
[3] X. Zhou, X. Hu, J. Yu, S. Liu, Z. Shu, Q. Zhang, H. Li, Y. Ma, H. Xu, T. Zhai, *Adv. Funct. Mater.* **2018**, *28*, 1706587.
[4] Y. Zhao, C. Zhang, D. D. Kohler, J. M. Scheeler, J. C. Wright, P. M. Voyles, S. Jin, *Science* **2020**, *370*, 442–445.
[5] X. Tong, Y. Zhao, Z. Zhuo, Z. Yang, S. Wang, Y. Liu, N. Lu, H. Li, T. Zhai, *Angew. Chem.* **2022**, *134*, e202112953.
[6] D. Ouyang, N. Zhang, Y. Li, T. Zhai, *Adv. Funct. Mater.* **2023**, *33*, 2208321.
[7] B. Tang, B. Che, M. Xu, Z. P. Ang, J. Di, H.-J. Gao, H. Yang, J. Zhou, Z. Liu, *Small Structures* **2021**, *2*, 2000153.
[8] A. Krzton-Maziopa, *Front. Chem.* **2021**, *9*.
[9] M. V. Roslova, O. I. Lebedev, I. V. Morozov, S. Aswartham, S. Wurmehl, B. Büchner, A. V. Shevelkov, *Inorg. Chem.* **2013**, *52*, 14419–14427.
[10] A. Navarro-Quezada, T. Devillers, T. Li, A. Bonanni, *Appl. Phys. Lett.* **2012**, *101*, 081911.
[11] R. N. Gannon, D. M. Hamann, J. Ditto, G. Mitchson, S. R. Bauers, D. R. Merrill, D. L. Medlin, D. C. Johnson, *ACS Appl. Nano Mater.* **2021**, *4*, 7943–7953.
[12] C. Zhao, Z. Li, T. Fan, C. Xiao, Y. Xie, *Research* **2020**, *2020*, ID 9652749 DOI 10.34133/2020/9652749.
[13] T. Dietl, K. Sato, T. Fukushima, A. Bonanni, M. Jamet, A. Barski, S. Kuroda, M. Tanaka, P. N. Hai, H. Katayama-Yoshida, *Rev. Mod. Phys.* **2015**, *87*, 1311–1377.
[14] D. Usanmaz, P. Nath, C. Toher, J. J. Plata, R. Friedrich, M. Fornari, M. Buongiorno Nardelli, S. Curtarolo, *Chem. Mater.* **2018**, *30*, 2331–2340.
[15] R. Steffen, R. Schöllhorn, *Solid State Ion.* **1986**, *22*, 31–41.
[16] G. Inzelt, Z. Puskás, K. Németh, I. Varga, *J. Solid State Electrochem.* **2005**, *9*, 823–835.
[17] G. Inzelt, A. Róka, *Isr. J. Chem.* **2008**, *48*, 185–196.
[18] A. Koitzsch, C. Habenicht, E. Müller, M. Knupfer, B. Büchner, S. Kretschmer, M. Richter, J. van den Brink, F. Börrnert, D. Nowak, A. Isaeva, Th. Doert, *Phys. Rev. Mater.* **2017**, *1*, 052001.
[19] R. Schöllhorn, R. Steffen, K. Wagner, *Angew. Chem. Int. Ed.* **1983**, *22*, 555–556.
[20] M. Roslova, E. Vinokurova, T. Thersleff, K. Kumar Bestha, S. Schwamborn, P. Machata, S. Schiemenz, A. Ovchinnikov, S. Avdoshenko, B. Rasche, A. Popov, A. U. B. Wolter, B. Büchner, A. Isaeva, *Manuscript in preparation* **2023**.
[21] M. Roslova, T. Thersleff, E. Vinokurova, S. Avdoshenko, A. Isaeva, *Acta Crystallogr.* **2021**, A 77, p. C79.
[22] W. Wan, J. Sun, J. Su, S. Hovmöller, X. Zou, *J. Appl. Crystallogr.* **2013**, *46*, 1863–1873.
[23] G. J. Wessel, D. J. W. Ijdo, *Acta Crystallogr.* **1957**, *10*, 466–468.
[24] R. A. D. Wentworth, R. Saillant, R. B. Jackson, W. E. Streib, K. Folting, *Inorg. Chem.* **1971**, *10*, 1453–1457.
[25] J. Darriet, *Rev. Chim. Miner.* **1981**, *18*, 27–32.
[26] V. T. Coombe, G. A. Heath, T. A. Stephenson, D. K. Vattis, *J. Chem. Soc. Dalton Trans.* **1983**, *10*, 2307–2309.
[27] B. D. Yeomans, D. G. Humphrey, G. A. Heath, *J. Chem. Soc. Dalton Trans.* **1997**, *22*, 4153–4166.
[28] A. M. Greenaway, *Vibrational Studies of (MLX5)n- Type Compounds*, University of Canterbury, **1976**.
[29] S. Hartwig, *Synthese und Charakterisierung von ternären Halogeniden und Oxidhalogeniden der Übergangsmetalle*, Universität Bayreuth, **2003**.
[30] P. A. Karplus, K. Diederichs, *Science* **2012**, *336*, 1030–1033.
[31] M. Grönke, P. Schmidt, M. Valldor, S. Oswald, D. Wolf, A. Lubk, B. Büchner, S. Hampel, *Nanoscale* **2018**, *10*, 19014–19022.
[32] R. D. Johnson, S. C. Williams, A. A. Haghighirad, J. Singleton, V. Zapf, P. Manuel, I. I. Mazin, Y. Li, H. O. Jeschke, R. Valentí, R. Coldea, *Phys. Rev. B* **2015**, *92*, 235119.
[33] S. Froeschke, K.-G. Schroth, U. Steiner, A. Popov, S. Schiemenz, D. Wolf, L. Giebeler, N. Gräßler, B. Büchner, P. Schmidt, S. Hampel, *2D Mater.* **2023**, *10*, 035011.
[34] R. Hentrich, A. U. B. Wolter, X. Zotos, W. Brenig, D. Nowak, A. Isaeva, T. Doert, A. Banerjee, P. Lampen-Kelley, D. G. Mandrus, S. E. Nagler, J. Sears, Y.-J. Kim, B. Büchner, C. Hess, *Phys. Rev. Lett.* **2018**, *120*, 117204.
[35] C. Wellm, J. Zeisner, A. Alfonsov, A. U. B. Wolter, M. Roslova, A. Isaeva, T. Doert, M. Vojta, B. Büchner, V. Kataev, *Phys. Rev. B* **2018**, *98*, 184408.
[36] S. Froeschke, D. Wolf, M. Hantusch, L. Giebeler, M. Wels, N. Gräßler, B. Büchner, P. Schmidt, S. Hampel, *Nanoscale* **2022**, *14*, 10483–10492.
[37] M. Roslova, S. Smeets, B. Wang, T. Thersleff, H. Xu, X. Zou, *J. Appl. Crystallogr.* **2020**, *53*, 1217–1224.
[38] W. Kabsch, *Acta Crystallogr. Sect. D* **2010**, *66*, 125–132.
[39] G. M. Sheldrick, *Acta Crystallogr. Sect. A* **2008**, *64*, 112–122.
[40] G. M. Sheldrick, *Acta Crystallogr. Sect. A* **2015**, *71*, 3–8.
[41] O. V. Dolomanov, L. J. Bourhis, R. J. Gildea, J. a. K. Howard, H. Puschmann, *J. Appl. Crystallogr.* **2009**, *42*, 339–341.
[42] K. Koepernik, H. Eschrig, *Phys. Rev. B* **1999**, *59*, 1743–1757.
[43] J. P. Perdew, Y. Wang, *Phys. Rev. B* **1992**, *45*, 13244–13249.
[44] M. Majumder, M. Schmidt, H. Rosner, A. A. Tsirlin, H. Yasuoka, M. Baenitz, *Phys. Rev. B* **2015**, *91*, 180401.
[45] K. W. Plumb, J. P. Clancy, L. J. Sandilands, V. V. Shankar, Y. F. Hu, K. S. Burch, H.-Y. Kee, Y.-J. Kim, *Phys. Rev. B* **2014**, *90*, 041112.

Manuscript received: June 26, 2023
Revised manuscript received: August 3, 2023
Accepted manuscript online: August 7, 2023

